Applied Catalysis B: Environmental 307 (2022) 121162

Contents lists available at ScienceDirect

Applied Catalysis B: Environmental

journal homepage: www.elsevier.com/locate/apcatb

Interfacial chemical bond modulated $Bi_{19}S_{27}Br_3$/g-C_3N_4 Z-scheme heterojunction for enhanced photocatalytic CO_2 conversion

Junze Zhao [a], Mengxia Ji [a], Hailong Chen [b], Yu-Xiang Weng [b], Jun Zhong [c], Yingjie Li [a], Shengyao Wang [d], Ziran Chen [e], Jiexiang Xia [a,*], Huaming Li [a]

[a] School of Chemistry and Chemical Engineering, Institute for Energy Research, Jiangsu University, 301 Xuefu Road, Zhenjiang 212013, PR China
[b] Beijing National Laboratory for Condensed Matter Physics, CAS Key Laboratory of Soft Matter Physics, Institute of Physics, Chinese Academy of Sciences, Beijing 100190, PR China
[c] Institute of Functional Nano & Soft Materials, Soochow University, Suzhou 215123, PR China
[d] College of Science, Huazhong Agricultural University, Wuhan 430070, PR China
[e] Department of Architecture and Environment Engineering, Sichuan Vocational and Technical College, Suining, Sichuan 629000, PR China

ARTICLE INFO

Keywords:
Z-scheme
$Bi_{19}S_{27}Br_3$/g-C_3N_4
Chemical bond
CO_2 photoreduction
Charge transfer

ABSTRACT

Direct Z-scheme heterojunction can primely facilitate separation efficiency of the photogenerated carriers and maximize the redox ability of as-prepared photocatalyst, which has been regarded as one of the promising strategies to increase photocatalytic CO_2 conversion efficiency. Herein, a novel interfacial C-S bond modulated Z-scheme heterojunction $Bi_{19}S_{27}Br_3$/g-C_3N_4 composite is constructed to accelerate the photogenerated electron transfer from g-C_3N_4 to $Bi_{19}S_{27}Br_3$, offering much more excited reductive electrons to the surface of $Bi_{19}S_{27}Br_3$ where owns lower CO_2 adsorption energy, which is more conducive to CO_2 reduction conversion. Without adding sacrificial agent or photosensitizer, the photocatalytic CO_2 conversion to CO yield of $Bi_{19}S_{27}Br_3$/g-C_3N_4 reaches up to 12.87 μmol g^{-1} h^{-1}, which is 5 and 4-fold of $Bi_{19}S_{27}Br_3$ and g-C_3N_4, respectively. This study provides the new insight in precisely tailoring photogenerated charge separation direction by establishing chemical bond in direct Z-scheme structure for CO_2 photoreduction.

1. Introduction

Excessive carbon dioxide released by fossil energy consumption has brought a series of environmental problems [1–4]. Inspired by natural photosynthesis, converting CO_2 into carbohydrates by artificial photosynthetic techniques is considered as a promising green approach to solve this matter [5–8]. However, it is still challenging for artificial photosynthesis to achieve high CO_2 conversion yield and selectivity under the present condition, which rest with the construction of efficient catalysts [1,7,8]. In addition, the poor charge separation efficiency and finite electron reducing capacity in the monocomponent system are also the two main decisive factors restricting the photocatalytic CO_2 conversion activity [9–12]. Thereinto, establishing suited semiconductor heterojunction with matched structure is deemed as an empirical strategy to cope with these challenges.

Graphitic carbon nitride (g-C_3N_4), as recently developed two-dimensional photocatalyst, possessing adjustable solar absorption range and energy band [13–15], has been universally acknowledged as the ideal photocatalyst for water splitting, water pollution treatment and carbon dioxide reduction in the last decade [16–19]. However, the photocatalytic activity of g-C_3N_4 still limited by the high recombination of electron-hole pairs due to the sluggish surface reaction kinetics, leading to low photocatalytic CO_2 conversion rate [20–25]. Up to now, great progress has been made to relieve this obstacle [24–29]. The construction of conventional type II semiconductor heterojunction with suitable energy band is considered as the feasible method to manipulate the efficiency of carrier separation [30–32]. Nevertheless, the charge-carriers redox capacity of this kind of heterojunctions was weaken with compromise of the high potential charges of g-C_3N_4 materials [33–35]. Different from type II heterojunction, direct Z-scheme heterojunction can effectively increase the spatially separation efficiency of photogenerated electron-hole pairs and preserve their strong redox capacity [33,34]. However, in the traditional direct Z-scheme photocatalyst system, the interaction force existing in the two different semiconductors is mainly the weak physical adsorption and stack force [31,35,36]. To further improve the directional charge separation in the

* Corresponding author.
E-mail address: xjx@ujs.edu.cn (J. Xia).

https://doi.org/10.1016/j.apcatb.2022.121162
Received 13 November 2021; Received in revised form 9 January 2022; Accepted 28 January 2022
Available online 1 February 2022
0926-3373/© 2022 Elsevier B.V. All rights reserved.

Z-scheme system, chemical bond-bridged Z-scheme heterojunctions have been reported recently, like Mo-S bond in S_v-$ZnIn_2S_4/MoSe_2$ [37], covalent bond in COF-368-TiO_2 [38], as well as In-O-Cd bond in $ZnIn_2S_4$/CdS [39]. These chemical bond-bridged Z-scheme structures could remarkably accelerate separation and transfer of the photogenerated charge carriers, inhibiting recombination of the separated carriers [37–39]. Therefore, establishing a chemical bond-bridged g-C_3N_4-based Z-scheme heterojunction is expected to be a potential strategy for the preparation of high-performance photocatalysts. However, only few works for the g-C_3N_4-based chemical bonds Z-scheme heterojunction have been reported [40]. The hinge on fabrication of g-C_3N_4-based Z-scheme structure bridging via chemical bonding is seeking a suitable semiconductor material with matched energy band.

$Bi_{19}S_{27}Br_3$ as a metal chalcohalide has excellent conductivity, high light adsorption ability and sufficiently negative conduction band (CB) position, guaranteeing the photoexcited electrons with strong reduction ability [41–44]. These intrinsic characteristics make $Bi_{19}S_{27}Br_3$ show great application prospect in CO_2 photoreduction study [44]. However, the unduly narrowed band gap of $Bi_{19}S_{27}Br_3$ (~ 1.48 eV) causes a high photogenerated charge carriers recombination rate, that critically affects the photocatalytic performance [41,42,45,46]. Compare with valence band (VB) of g-C_3N_4 (~ 1.73 eV), the VB position of $Bi_{19}S_{27}Br_3$ is much more negative (~ 0.18 eV) which even closer to CB of g-C_3N_4 (~ −0.84 eV). Therefore, it can be expected that establishing direct Z-scheme heterojunction between $Bi_{19}S_{27}Br_3$ and g-C_3N_4 materials would definitely improve the transition efficiency of the interfacial charge carriers, also maximize reduction capability of excited electrons.

Based on the aforementioned advantages, a novel Z-scheme $Bi_{19}S_{27}Br_3$/g-C_3N_4 heterojunction bridging via C-S bonds was fabricated. The C-S bonds between $Bi_{19}S_{27}Br_3$ and g-C_3N_4 acted as an interfacial charge migration channel, accelerating the transition efficiency of interfacial electron from g-C_3N_4 to $Bi_{19}S_{27}Br_3$, thus guaranteeing much more excited electrons participating in the CO_2 photoreduction reaction. Without extra photosensitizer and sacrificial agent, the CO yield of $Bi_{19}S_{27}Br_3$/g-C_3N_4-5 Z-scheme heterojunction was 12.87 μmol g^{-1} h^{-1}, which is 5 and 4-folds as higher as that of $Bi_{19}S_{27}Br_3$ and g-C_3N_4, respectively. As the results, the chemical bond Z-scheme heterojunction improved the CO_2 photoreduction capacity effectively, which provides the new insight in precisely tailoring photogenerated charge separation direction for the high performance photocatalysts.

2. Experimental

2.1. The chemicals and materials

All the materials applied for experiments were analytical reagent and used without any purification. The ionic liquid 1-hexadecyl-3-methylimidazolium bromide ([C_{16}mim]Br) was purchased from Lanzhou Institute of Chemical Physics, Chinese Academy of Sciences.

2.2. Materials preparation

2.2.1. The synthesis of g-C_3N_4 material

The g-C_3N_4 was synthesized by the three-step calcination method. 2 g dicyandiamide was put into the crucible and calcined in a tube furnace; the temperature was raised to 350 ℃ in 90 min and maintained for 2 h. Then the temperature was raised to 600 ℃ in 90 min and kept for another 2 h. After that, the yellow powder was obtained and prepared for the next experiment. 1 g yellow g-C_3N_4 was prepared for the next calcining process in muffle furnace. After the further 2 h calcining at 550 ℃, the pale-yellow g-C_3N_4 powder will carry out. Finally, the 1 g pale yellow g-C_3N_4 was calcined at 500 ℃ for another 2 h and the white-color g-C_3N_4 was obtained.

2.2.2. The preparation of $Bi_{19}S_{27}Br_3$/g-C_3N_4 and $Bi_{19}S_{27}Br_3$ materials

The $Bi_{19}S_{27}Br_3$/g-C_3N_4-5 composite is applied as an example to discuss the preparation of the composite materials. Above all, the 0.0350 g thiourea, 0.1549 g [C_{16}mim]Br and 0.008 g $Bi(NO_3)_3$•$5H_2O$ were dispersed in 20 mL glycol. After that, 0.0836 g g-C_3N_4 was added into the mixture and stirred for 30 min. Then the mixture was poured into a 25 mL Teflon-lined autoclave and heated at 130 ℃ for 12 h. After cooled down to room temperature, the gray-color powder was centrifuged and washed by alcohol and distilled water. Finally, the powder was dried at 60 ℃ for 12 h in the vacuum environment and the $Bi_{19}S_{27}Br_3$/g-C_3N_4-5 composite could be obtained. The $Bi_{19}S_{27}Br_3$/g-C_3N_4-1, 3, 7 composites were synthesized by the same method with different added contents of g-C_3N_4 (0.4356 g, 0.1423 g and 0.0584 g, respectively). The pure $Bi_{19}S_{27}Br_3$ nanorod was also synthesis with the same condition without adding g-C_3N_4 and the color was black.

2.2.3. The synthesis of $Bi_{19}S_{27}Br_3$/g-C_3N_4-M materials

The 95 mg g-C_3N_4 and 5 mg as-prepared $Bi_{19}S_{27}Br_3$ materials were mixed and transferred into an agate mortar. After strong grinding for 30 min, the uniform gray powder was obtained, which was named as $Bi_{19}S_{27}Br_3$/g-C_3N_4-M materials.

2.3. Characterizations

The X-ray diffraction spectra (XRD) was carried out by a Shimadzu XRD-6000 X-ray diffractometer (the monochromatized Cu- Kα radiation was applied). The morphologies of as-prepared materials were carried out by a JEOL-JSM-7001F scanning electron microscope (SEM) and a JEOL-JEM-2010 transmission electron microscopy (TEM) with the energy dispersive X-ray spectroscope. The X-ray photoelectron spectroscopy (XPS) spectra were measured on the a PHI5300 with a monochromatic Mg Kα source. The Fourier transform infrared spectroscopy (FT-IR) and diffuse reflectance infrared Fourier transform spectroscopy (DRIFTS) were detected by the Nicolet Model Nexus 470 FT-IR equipment. The UV–vis diffuse reflectance spectra (DRS) were measured on the Shimadzu UV-2450 UV–vis spectrophotometer. The Bi L_3-edge X-ray absorption near-edge structure (XANES) spectra and extended X-ray absorption fine structure spectroscopy (EXAFS) were measured by the Beamline 11B at Shanghai Synchrotron Radiation Facility (SSRF). All the electrochemical experiments were proceeded by the CHI 760E electrochemical system (Chenhua Instrument Company). The femtosecond amplifier laser system (Hurricane, Spectra Physics) was applied to measure the ultrafast spectra of as-prepared materials, and an optical fiber spectrometer (AvaSpec-ULS2048CL-EVO, Avantes) was employed to detect the excitation-induced transmission change of the probe light.

A gas chromatography-mass spectrometry (6890N Network GC system, Agilent Technologies, USA) was applied to carry out isotope-labeling experiments with $^{13}CO_2$ gas as the carbon source. During this process, the two kinds of chromatographic columns were applied to detect ^{13}CO (HP-MOLESIEVE, 30 m × 0.32 mm × 25 μm, Agilent Technologies, USA) and $^{13}CO_2$ (HP-PLOT/Q, 30 m × 0.32 mm×20 μm, Agilent Technologies, USA) in the gas product with the same condition.

An in-situ diffuse reflectance infrared Fourier transform spectroscopy (DRIFTS) (Thermo fisher Nicolet iZ10, USA) was employed to analysis the CO_2 photoreduction process of $Bi_{19}S_{27}Br_3$/g-C_3N_4-5 material. The helium gas was applied to clean the material at 120 °C. After that, the material was first measured without the irradiation of light at first (background). Then the H_2O vapor and CO_2 were introduced and kept for 30 min to achieve the adsorption-desorption equilibrium of gas and material. Finally, the DRIFTS spectrum was measure under the irradiation of light with different times.

2.4. Measurement of photocatalytic activity

The CO_2 photoreduction equipment (Perfectlight Labsolar-6A plus) was employed to verify the CO_2 photoreduction activities of as-prepared materials. The 0.03 g catalyst was mixed with 50 mL water in a reactor

and drained of air. Then put in a certain amount of CO_2 for the 30 min dark adsorption process. The temperature and the pressure of the reaction bottle were kept at 5 °C and 80 KPa, respectively. Then turn on the Xe light (300 W, PLS-SXE 300D, Perfectlight, China) as a simulated solar source. Finally, a portion of the produced gas is injected into the gas chromatography (Zhejiang FuLi Chromatograph Instruments Co., ltd. GC-9790II) per hour to analyze the yield of CO and O_2 with the flame ionization detector (FID) and thermal conductivity detector (TCD), respectively.

2.5. The density functional theory (DFT) calculation

The DFT calculation was applied by using the *Vienna* abinitio *simulation package* (VASP) with the *projector augmented wave* (PAW) method. The *Perdew-Burke-Ernzerhof* (PBE) functional of *generalized gradient approximation* (GGA) was applied as the exchange–correlation functional. To simulate the g-C_3N_4, a one-layer g-C_3N_4 model with the (0 0 2) plane was constructed as slab and the vacuum layer was 10 Å. To improve the calculation accuracy and efficiency, a $Bi_{19}S_{27}Br_3$ cluster model (Bi: S: Br = 19: 27: 3) was placed beyond the surface of g-C_3N_4 slab to simulate the $Bi_{19}S_{27}Br_3$/g-C_3N_4 composite. For the destiny of state (DOS) calculations of g-C_3N_4 and $Bi_{19}S_{27}Br_3$ models, the K-point was set as 9 × 9 × 9 and 0 × 0 × 0 × 1, respectively. The cut-off energy was set as 420 eV. To calculate the theoretical adsorption energy (E_{ads}), a CO_2 molecule was placed beyond the surface of model to simulate the adsorption process of CO_2 molecule. The cut-off energy was 420 eV and the K-point of g-C_3N_4 and $Bi_{19}S_{27}Br_3$/g-C_3N_4 were set as 3 × 3 × 1 while that of $Bi_{19}S_{27}Br_3$ was 0 × 0 × 0 × 1. The energy convergence criteria were set at 1×10^{-4} eV per atom and the force convergence criteria were set as − 0.05 eV $Å^{-1}$. The adsorption energy calculation was according to the equation:

$$E_{ads} = E_{total} - E_{slab} - E_{gas}$$

Among it, the E_{total}, E_{slab} and E_{gas} were the energy of slab with CO_2 molecule, slab and CO_2 molecule, respectively. Finally, the theoretical E_{ads} of g-C_3N_4, $Bi_{19}S_{27}Br_3$ and $Bi_{19}S_{27}Br_3$/g-C_3N_4 composite could be carried out.

3. Results and discussion

3.1. The design, synthesis and the characteristic of $Bi_{19}S_{27}Br_3$/g-C_3N_4 composites

One of the keys to construct Z-scheme heterojunction is the suitable band structures of the two semiconductors. The DOS calculation was applied to analysis the band structures of $Bi_{19}S_{27}Br_3$, g-C_3N_4 and $Bi_{19}S_{27}Br_3$/g-C_3N_4. As shown in Fig. S1 and Fig. S2, the band-gap of g-C_3N_4 is larger than that of $Bi_{19}S_{27}Br_3$. Clearly, the VB and CB of g-C_3N_4

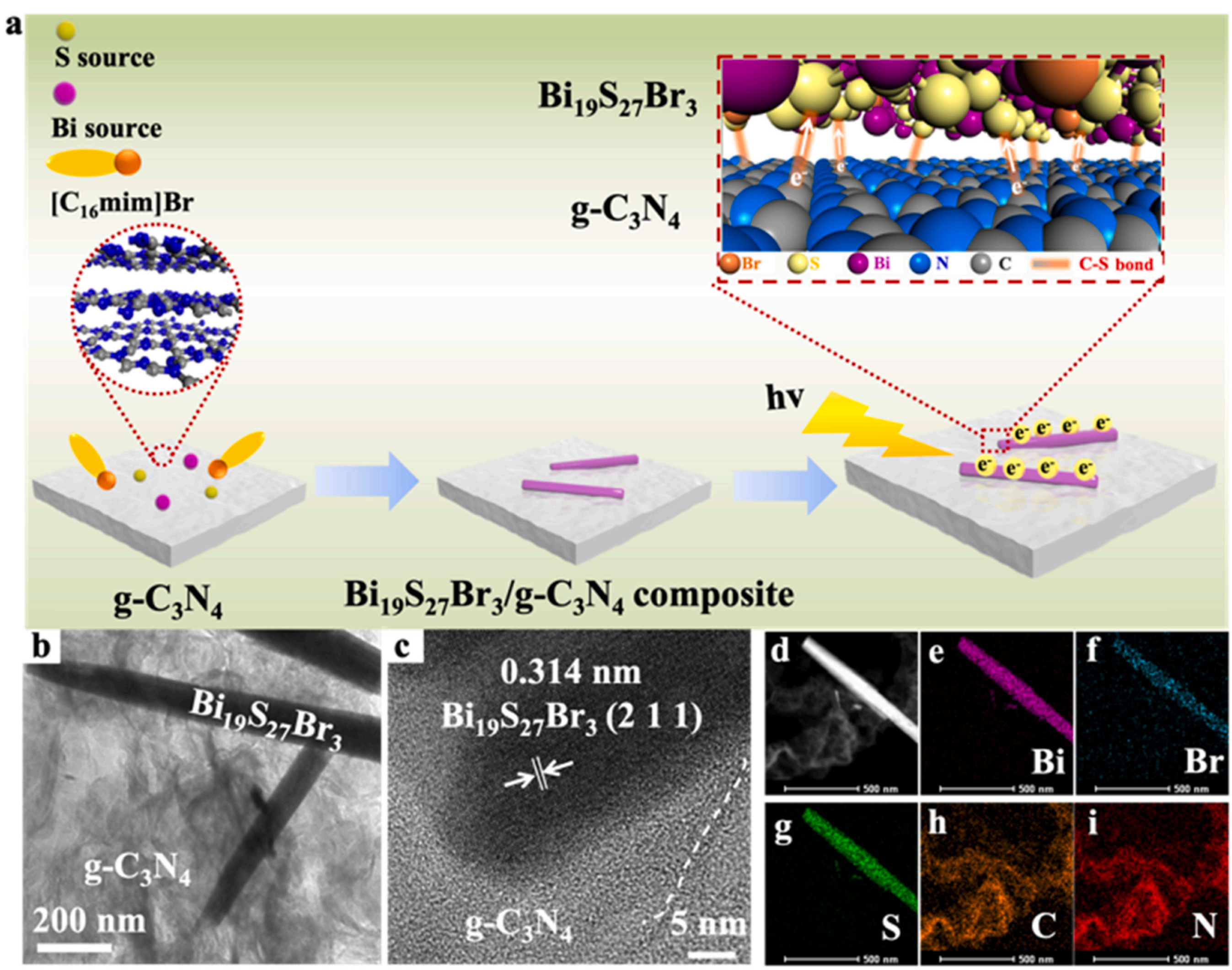

Fig. 1. (a) The schematic illustration for the preparation and CO_2 photoreduction process of the $Bi_{19}S_{27}Br_3$/g-C_3N_4-5 composite. (b) TEM and (c) HRTEM results of $Bi_{19}S_{27}Br_3$/g-C_3N_4-5 composite. (d-i) Elemental mapping images of $Bi_{19}S_{27}Br_3$/g-C_3N_4-5 material.

are constructed by N and the C element [47]. Besides, the VB and CB of the $Bi_{19}S_{27}Br_3$ are mainly dominated by S and Bi elements, respectively. According to the band structure, a Z-scheme heterojunction can be formed by establishing an electron transport channel between the VB of $Bi_{19}S_{27}Br_3$ and CB of g-C_3N_4. A chemical bond between the VB of $Bi_{19}S_{27}Br_3$ and CB of g-C_3N_4 materials may build with the generation of CS bonds (C-S or C═S), which can act as the interfacial charge migration pathway for the photogenerated electron and ensure the striking charge transfer efficiency between two semiconductors. Thus, Z-scheme $Bi_{19}S_{27}Br_3$/g-C_3N_4 composites based on the CS bond may exhibited the promising high-efficiency CO_2 photoreduction capacity. On the other hand, the DOS of $Bi_{19}S_{27}Br_3$/g-C_3N_4 was constructed by the DOS of g-C_3N_4 and $Bi_{19}S_{27}Br_3$. No other new state appeared in the result of $Bi_{19}S_{27}Br_3$/g-C_3N_4.

By using the reactive ionic liquids assisted solvothermal method, the $Bi_{19}S_{27}Br_3$/g-C_3N_4 was successfully synthesized. In Fig. 1**a**, the forming process of $Bi_{19}S_{27}Br_3$/g-C_3N_4 composites is illustrated. The SEM and TEM (as shown in Fig. S3a and Fig. S3b) of $Bi_{19}S_{27}Br_3$ material show the uniform nanorods structure with the diameter of 50–100 nm. The high-resolution transmission electron microscope (HRTEM) of $Bi_{19}S_{27}Br_3$ nanorods (Fig. S3c) shows that the lattice fringe is calculated as 0.314 nm matching with the (211) crystal plane of $Bi_{19}S_{27}Br_3$ material (JCPDS card No.26-0813). Besides, the selected area electron diffraction (SAED) pattern illustrates that the crystal phase of as-prepared $Bi_{19}S_{27}Br_3$ material belongs to single-crystal (Fig. S3d).

The SEM (Fig. S4) and TEM (Fig. 1**b**) results of $Bi_{19}S_{27}Br_3$/g-C_3N_4-5 revealed that the $Bi_{19}S_{27}Br_3$ nanorod is loaded on the surface of g-C_3N_4, and the morphologies of $Bi_{19}S_{27}Br_3$ and g-C_3N_4 maintained completely. The HRTEM image (Fig. 1**c**) and the elemental mapping results of $Bi_{19}S_{27}Br_3$/g-C_3N_4-5 composite (Fig. 1**d**-1**i**) indicated tight contact between two materials. The XRD were applied to reveal the phase and crystal of the materials. In Fig. 2**a**, it can be observed that all diffraction peaks of the $Bi_{19}S_{27}Br_3$/g-C_3N_4 composites can be well matched with the standard phase of $Bi_{19}S_{27}Br_3$ material (JCPDS card No.26-0813) and g-C_3N_4 [25], indicating the successful preparation of $Bi_{19}S_{27}Br_3$/g-C_3N_4 materials. The FT-IR spectroscopy of the as-prepared materials (Fig. S5) further confirmed the successful synthesis of $Bi_{19}S_{27}Br_3$/g-C_3N_4.

3.2. The insight of chemical bond between $Bi_{19}S_{27}Br_3$ and g-C_3N_4

To explore the chemical bonding between the two materials, the XPS (Fig. S6) was executed to reveal the chemical components of the as-

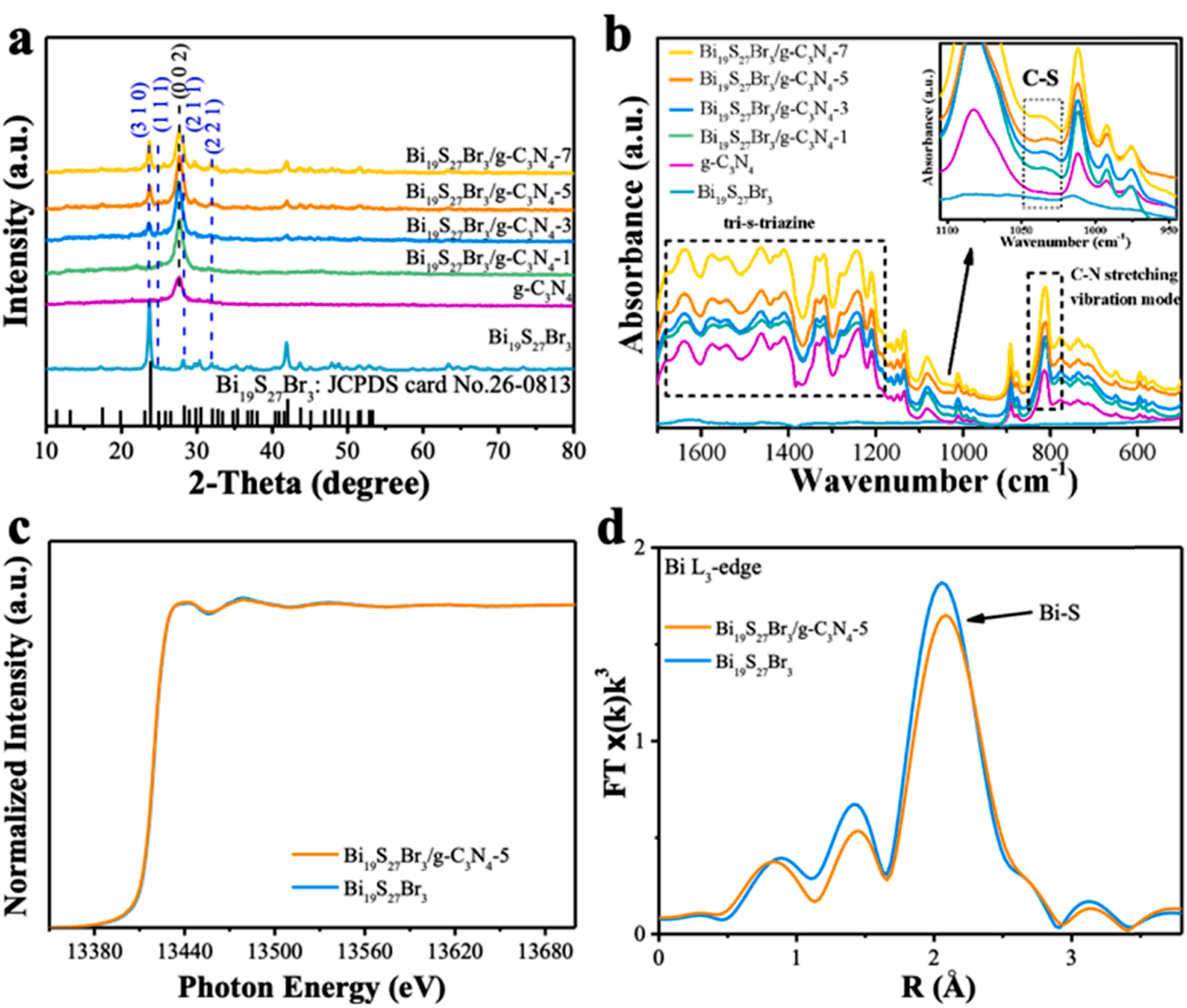

Fig. 2. (a) The XRD patterns of $Bi_{19}S_{27}Br_3$/g-C_3N_4 composites, $Bi_{19}S_{27}Br_3$ and g-C_3N_4 materials. (b) DRIFTS spectra of $Bi_{19}S_{27}Br_3$/g-C_3N_4 composites, pure $Bi_{19}S_{27}Br_3$ and pure g-C_3N_4. (c) Bi L_3-edge XANES and (d) Fourier transformed EXAFS spectra of $Bi_{19}S_{27}Br_3$/g-C_3N_4-5 and $Bi_{19}S_{27}Br_3$ materials.

prepared materials. Comparing with the g-C_3N_4, the C 1 s of $Bi_{19}S_{27}Br_3$/g-C_3N_4-5 composite exhibits a striking positive shift. Besides, both Bi 4 f and S 2p of $Bi_{19}S_{27}Br_3$/g-C_3N_4-5 composite show obviously negative shifts compared with $Bi_{19}S_{27}Br_3$. All these results indicated the strong interaction between $Bi_{19}S_{27}Br_3$ and g-C_3N_4 materials. The DRIFTS was employed to further figure out the force between $Bi_{19}S_{27}Br_3$ and g-C_3N_4. In Fig. 2**b**, a new peak locating at about 1038 cm^{-1} can be attributed to the C-S stretching vibration [48].

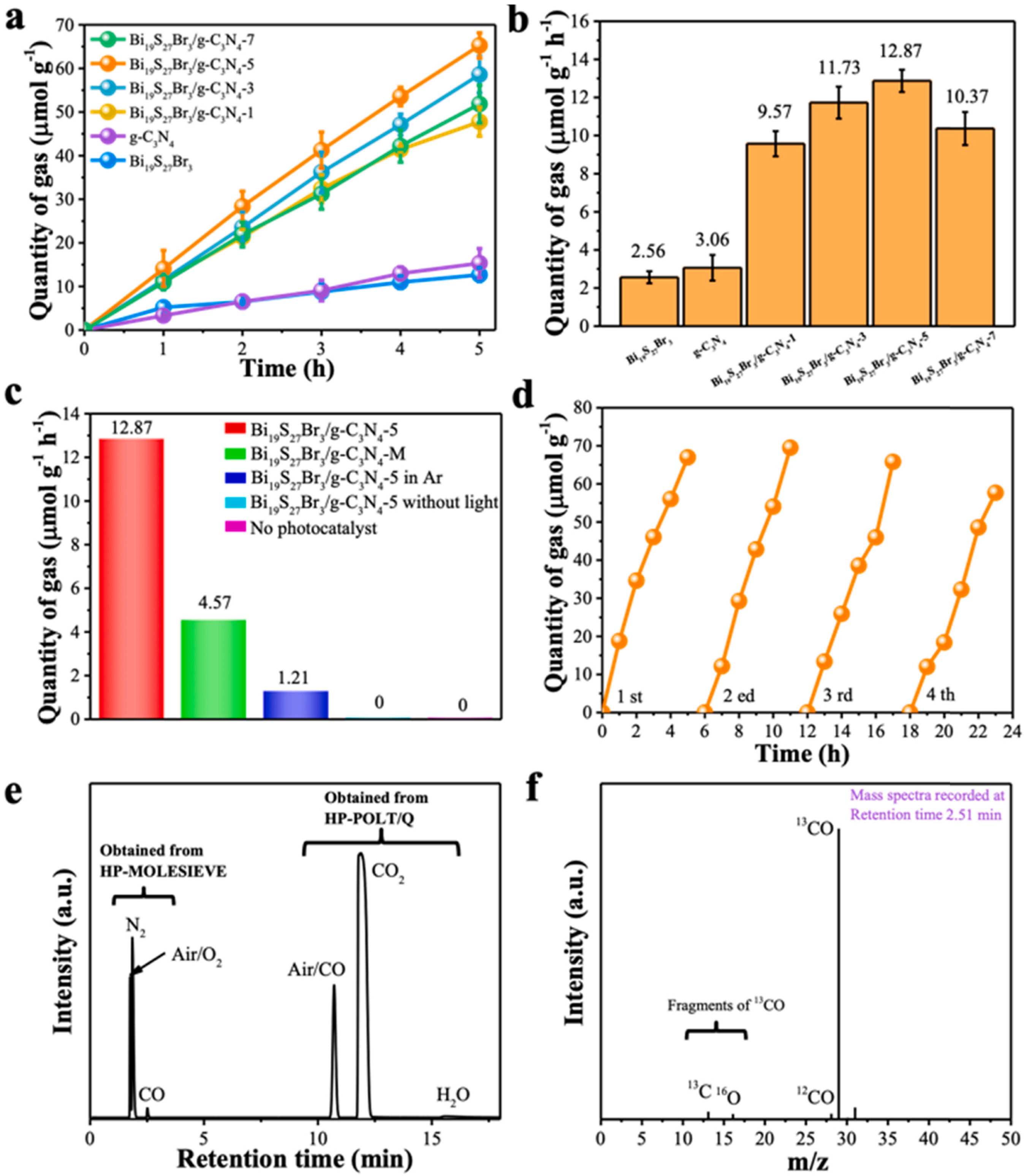

Fig. 3. (a) The time courses of photocatalytic CO evolution and (b) the CO_2 photoreduction rate in 5 h using $Bi_{19}S_{27}Br_3$, g-C_3N_4 and $Bi_{19}S_{27}Br_3$/g-C_3N_4 materials as photocatalysts. (c) The CO_2 photoreduction experiments of the $Bi_{19}S_{27}Br_3$/g-C_3N_4-5 composite, $Bi_{19}S_{27}Br_3$/g-C_3N_4-M, the $Bi_{19}S_{27}Br_3$/g-C_3N_4-5 composite in Ar, the $Bi_{19}S_{27}Br_3$/g-C_3N_4-5 without light and without photocatalyst. (d) The stability of $Bi_{19}S_{27}Br_3$/g-C_3N_4-5 composite. (e) The total ion chromatography and (f) mass spectra of ^{13}CO obtained from HP-MOLESIEVE in the photocatalytic reduction of $^{13}CO_2$.

In order to detect whether other chemical bonds were generated, the local electronic structure and coordination environment of Bi in $Bi_{19}S_{27}Br_3$/g-C_3N_4-5 were investigated by X-ray absorption measurement. In Fig. 2**c**, the L_3-edge XANES spectra of $Bi_{19}S_{27}Br_3$/g-C_3N_4-5 and $Bi_{19}S_{27}Br_3$ reveal that no interaction generated on Bi atoms between g-C_3N_4 and $Bi_{19}S_{27}Br_3$ materials. The main peak at 2.2 Å is assigned to the Bi-S bond of $Bi_{19}S_{27}Br_3$ in the results of EXAFS (Fig. 2**d**) [49]. However, the signal intensity of $Bi_{19}S_{27}Br_3$/g-C_3N_4-5 composite is clearly weaker than that of pure $Bi_{19}S_{27}Br_3$, revealing the low coordination number of Bi-S bonds [50]. All these results indicated the different local atomic arrangement of $Bi_{19}S_{27}Br_3$/g-C_3N_4-5 relative to the $Bi_{19}S_{27}Br_3$ [50]. Combining with the results of DRIFTS and XPS, the decrease of coordination number of Bi-S bonds can be attributed to the formation of C-S bonds.

3.3. The CO_2 photoreduction performance of as-prepared materials

The photocatalytic CO_2 reduction performance of these materials were carried out in water environment at 5 ℃ (Fig. 3**a**). As shown in Fig. 3**b**, the reaction rates were also calculated to visualize the photocatalytic activities of materials. After 5 h Xe lamp irradiation, the pure $Bi_{19}S_{27}Br_3$ and g-C_3N_4 exhibit the poor photocatalytic CO yield which are about 12.82 and 15.30 μmol g^{-1} with reaction rate of 2.56 and 3.06 μmol g^{-1} h^{-1}, respectively. As expected, the $Bi_{19}S_{27}Br_3$/g-C_3N_4 composites exhibit the improved CO_2 photoreduction activity. The $Bi_{19}S_{27}Br_3$/g-C_3N_4-5 shows the highest CO yield which is 64.35 μmol g^{-1} (12.87 μmol g^{-1} h^{-1}), and is almost 5 and 4-folds yield of $Bi_{19}S_{27}Br_3$ and g-C_3N_4. Besides, the O_2 can be also detected which yield rate is about 6.12 μmol g^{-1} h^{-1} as shown in Fig. S7. To investigate the important role of C-S bonds during the CO_2 photoreduction process of the $Bi_{19}S_{27}Br_3$/g-C_3N_4 composites, the $Bi_{19}S_{27}Br_3$/g-C_3N_4-M catalyst was prepared by mechanical grinding method with the same mass rate. The XRD and SEM experiments identified that there is no significant difference for the crystal phase and the morphology of $Bi_{19}S_{27}Br_3$/g-C_3N_4-5 and $Bi_{19}S_{27}Br_3$/g-C_3N_4-M (As shown in Fig. S8). The DRIFTS was applied to confirm the generation of chemical bond. In Fig. S9, there is no C-S bonds generated in the $Bi_{19}S_{27}Br_3$/g-C_3N_4-M catalyst synthesized by mechanical grinding method. In Fig. 3**c**, the CO yield rate of $Bi_{19}S_{27}Br_3$/g-C_3N_4-M is about 4.57 μmol g^{-1} h^{-1} which is much lower than that of $Bi_{19}S_{27}Br_3$/g-C_3N_4-5 composite. That identified the C-S bonds play an important role in improving CO_2 photoreduction activity of the $Bi_{19}S_{27}Br_3$/g-C_3N_4-5 composite. Several control experiments were performed to ascertain the C source of the CO product. The photocatalytic activities are obviously inhibited under given conditions including no light, no photocatalyst or in Ar atmosphere during the CO_2 reduction process, indicating the CO is only produced by the photocatalytic CO_2 reduction reaction (Fig. 3**c**). To figure out the C source of CO, the $^{13}CO_2$ gas was applied as the carbon source for the CO_2 photoreduction of $Bi_{19}S_{27}Br_3$/g-C_3N_4-5 material. The results of isotope labeling measurement experiments are shown in Fig. 3**e** and **f**, the total ion chromatographic peak around 2.51 min (Obtained from HP-MOLESIEVE) can be assigned to the CO (Fig. 3**e**). Meanwhile, combining with the peak appears at $m/z = 29$ and the peaks of fragments produced (the peaks appeared at $m/z = 13$ and 16 can be attributed to the ^{13}C and O) in the mass spectra (Fig. 3**f**), it can be confirmed that the ^{13}CO is produced from $^{13}CO_2$ during the CO_2 photoreduction process [1]. The detailed is shown in Fig. S10. The further isotope experiment was sufficient to prove that the carbon source of CO is CO_2. In Fig. 3**d**, the CO_2 photoreduction stability of $Bi_{19}S_{27}Br_3$/g-C_3N_4-5 composite is investigated by the 4-times recycling CO_2 photoreduction experiments. The $Bi_{19}S_{27}Br_3$/g-C_3N_4-5 represents the strong stabilization of photocatalytic activity after the long-term photocatalytic experiments. Meanwhile, there are no significant changes in the SEM and XRD of $Bi_{19}S_{27}Br_3$/g-C_3N_4-5 composite after the recycling experiments (Fig. S11), indicating the excellent stability of the $Bi_{19}S_{27}Br_3$/g-C_3N_4-5.

3.4. Explore the cause of increased photocatalytic activity

Several experiments were carried out to further understand the reasons for the improvement of catalyst performance. According to the DRS (Fig. S12a), the light adsorption edge of $Bi_{19}S_{27}Br_3$/g-C_3N_4 composite performs a clear red shift than g-C_3N_4, which indicated the $Bi_{19}S_{27}Br_3$/g-C_3N_4 composite exhibits the enhancing capture capacity of visible light. The electrochemical impedance spectroscopy (Fig. S12c) further reveals a higher photogenerated charge transfer efficiency of $Bi_{19}S_{27}Br_3$/g-C_3N_4-5 material compared with $Bi_{19}S_{27}Br_3$ and g-C_3N_4. It can be assumed that the generation of C-S bond boosts the transfer of charge carriers between g-C_3N_4 and $Bi_{19}S_{27}Br_3$. In the results of photocurrent experiments (Fig. S12d), the photocurrent intensity of $Bi_{19}S_{27}Br_3$/g-C_3N_4-5 is higher than that of $Bi_{19}S_{27}Br_3$ and g-C_3N_4, which indicates that the generation of C-S bond accelerates the separation of photogenerated carriers effectively. On the other hand, the photocurrent intensity of $Bi_{19}S_{27}Br_3$/g-C_3N_4-M is quite lower than $Bi_{19}S_{27}Br_3$/g-C_3N_4-5. That means without the generation of C-S bond, the $Bi_{19}S_{27}Br_3$/g-C_3N_4-M cannot exhibit the higher separation efficiency of photogenerated carriers compared with the $Bi_{19}S_{27}Br_3$/g-C_3N_4-5, and further limited the CO_2 photoreduction capacity of $Bi_{19}S_{27}Br_3$/g-C_3N_4-M.

3.5. The CO_2 photoreduction process of $Bi_{19}S_{27}Br_3$/g-C_3N_4 composite

To further figure out the photocatalytic mechanism of $Bi_{19}S_{27}Br_3$/g-C_3N_4 composite and the role of C-S bonds in this system, several experiments were carried out to confirm the band structure, surface reaction and electron transfer process of as-prepared materials. The ultraviolet photoelectron spectrometer (UPS) was employed to measure the valence band potential (E_{VB}) and work function (Φ) of $Bi_{19}S_{27}Br_3$ and g-C_3N_4 materials. A sample based of −5 V was applied to observe the secondary electron cutoff (Fig. 4**a**). For the $Bi_{19}S_{27}Br_3$ material, the work function Φ is calculated as 21.22 – 17.85 = 3.37 eV (vs. vacuum). The VB top energy (vs. vacuum) can be calculated as –3.37 – 1.21 = –4.58 eV. Therefore, the E_{VB} of $Bi_{19}S_{27}Br_3$ material can be calculated as – (–4.58) – 4.4 = 0.18 V vs. normal hydrogen electrode (NHE). Because the E_g of $Bi_{19}S_{27}Br_3$ material is 1.48 eV (based on the calculation in Fig. S12b), the conduction band potential (E_{CB}) vs. NHE is calculated by E_{VB}- E_g = –1.30 V. Meanwhile, the E_{VB} vs. NHE and E_{CB} vs. NHE of g-C_3N_4 are calculated as 1.73 and −0.84 V. Besides, the Φ of g-C_3N_4 is determined to be 1.77 eV. The photocatalytic O_2 evolution reaction experiments of $Bi_{19}S_{27}Br_3$, g-C_3N_4, $Bi_{19}S_{27}Br_3$/g-C_3N_4-5 and $Bi_{19}S_{27}Br_3$/g-C_3N_4-M were further carried out to identify the electron charge transfer direction (As shown in Fig. S13, and the detail was shown in Supplementary information). As the E(CO_2/CO) and E(H_2O/O_2) are reported as – 0.53 and 1.23 V vs NHE [51,52], the VB of the $Bi_{19}S_{27}Br_3$ is negative than E(H_2O/O_2). Therefore, the pure $Bi_{19}S_{27}Br_3$ exhibits no O_2 evolution performance. It can be observed that the $Bi_{19}S_{27}Br_3$/g-C_3N_4-5 exhibits the higher O_2 evolution capacity than that of pure g-C_3N_4. Therefore, the type II heterojunction mechanism is impossible to generate for the $Bi_{19}S_{27}Br_3$/g-C_3N_4 composite due to the O_2 cannot be generated on the VB of $Bi_{19}S_{27}Br_3$ (As shown in Fig. S14). Combining with the DFT simulation and O_2 production during the CO_2 photoreduction process of $Bi_{19}S_{27}Br_3$/g-C_3N_4 material, a possible C-S bridged direct Z-scheme mechanism can be put forward.

As shown in Fig. 4**b**, when the light irradiates on the $Bi_{19}S_{27}Br_3$/g-C_3N_4 composite, the photogenerated electron gathers on the CB of $Bi_{19}S_{27}Br_3$ and g-C_3N_4. Subsequently, the electron on the CB of g-C_3N_4 transfers to $Bi_{19}S_{27}Br_3$ along the C-S bonds and recombines with the hole on the VB of $Bi_{19}S_{27}Br_3$. During this process, the C-S bond is acted as the “high-speed channel” for the transfer of photogenerated carriers. In this regard, more electron is gathered on the CB of $Bi_{19}S_{27}Br_3$ while the hole is gathered on g-C_3N_4 material’s VB, the CO can be generated on CB of $Bi_{19}S_{27}Br_3$. To further identify the electron transfer direction clearly, the chloroplatinic acid solution was applied to deposit the Pt particle on the $Bi_{19}S_{27}Br_3$/g-C_3N_4 material’s surface under the irradiation of light. After

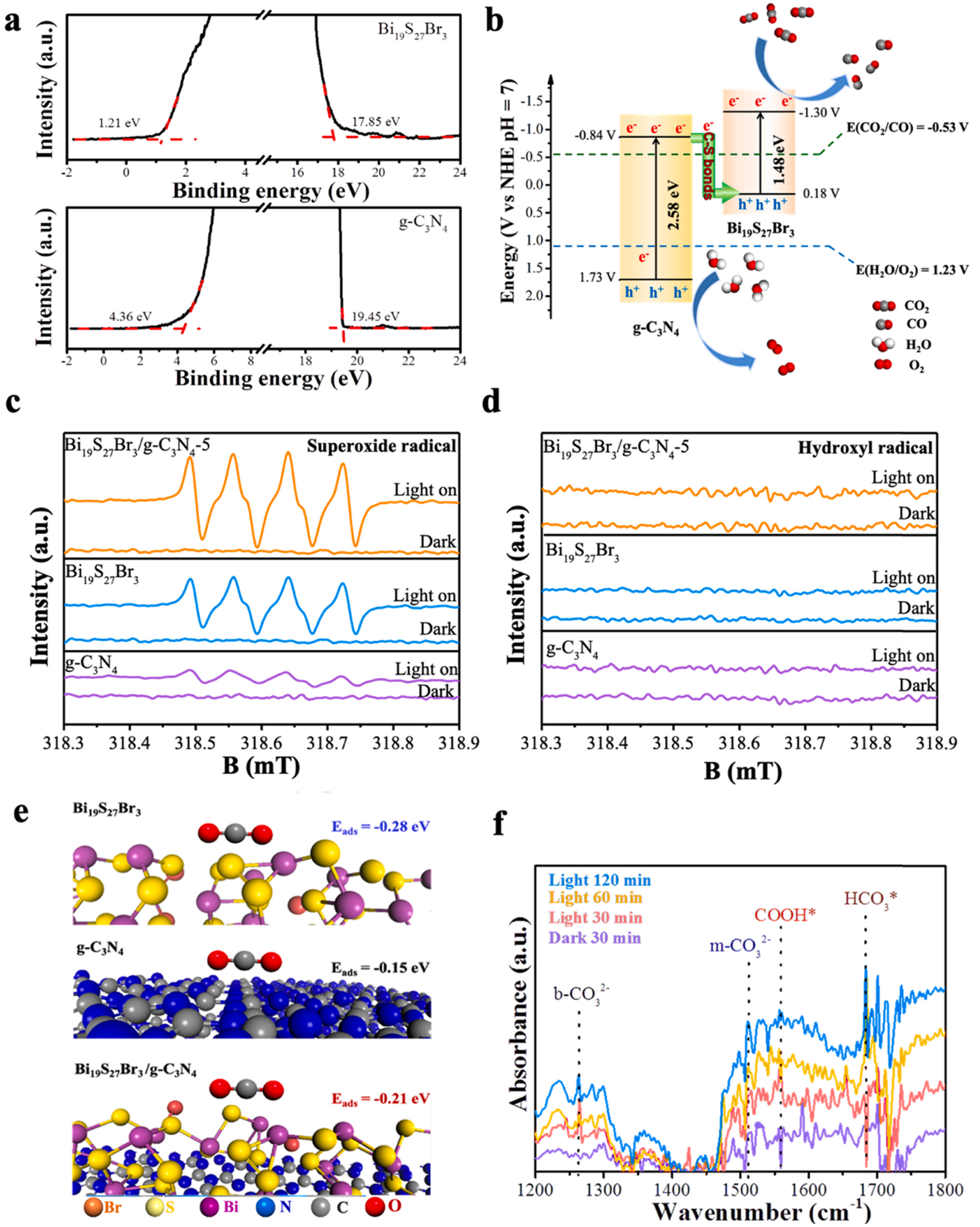

Fig. 4. (a) The UPS spectra of $Bi_{19}S_{27}Br_3$ and $g\text{-}C_3N_4$ materials. (b) The schematic of electron transmission by C-S bonds between $g\text{-}C_3N_4$ and $Bi_{19}S_{27}Br_3$. (c-d) The ESR spectra of $Bi_{19}S_{27}Br_3$, $g\text{-}C_3N_4$ and $Bi_{19}S_{27}Br_3/g\text{-}C_3N_4$ composite materials. (e) DFT calculations of adsorption energies for $Bi_{19}S_{27}Br_3$, $g\text{-}C_3N_4$ and $Bi_{19}S_{27}Br_3/g\text{-}C_3N_4$ composite. (f) The in-situ DRIFTS for the CO_2 photoreduction of $Bi_{19}S_{27}Br_3/g\text{-}C_3N_4$-5 composite.

Xe lamp light irradiation for 20 min, the TEM elements mapping images of $Bi_{19}S_{27}Br_3$/g-C_3N_4 composite exhibited the Pt particle is preferred to deposit on the $Bi_{19}S_{27}Br_3$ (Fig. S16), indicating the electron is preferred to gather on the $Bi_{19}S_{27}Br_3$ under the irradiation of light. Therefore, the photo-generated electron on the g-C_3N_4 transfers and accumulates to the surface of $Bi_{19}S_{27}Br_3$ effectively with the assistance of C-S bonds. Therefore, a typical Z-scheme mechanism can be carried out.

To further reveal the charge transfer process between the interface of $Bi_{19}S_{27}Br_3$ and g-C_3N_4, the electron spin resonance (ESR) spectra of $Bi_{19}S_{27}Br_3$, g-C_3N_4 and $Bi_{19}S_{27}Br_3$/g-C_3N_4-5 composite were carried out. The 5,5-dimethyl-1-pyrroline N-oxide (DMPO) was applied as a spin trap. The Fig. 4 **c** and **d** show the results of DMPO-$\cdot O_2^-$ and DMPO-$\cdot$OH. According to the previous reports, the $E(O_2/\cdot O_2^-)$ is − 0.33 V (vs. NHE) and the $E(\cdot OH/OH^-)$ is 2.38 V (vs. NHE) [53]. Since the VB of $Bi_{19}S_{27}Br_3$ and g-C_3N_4 are more positive than $E(\cdot OH/OH^-)$, both of them cannot generate the$\cdot$OH during the photocatalytic activity. On the other hand, both of them can detect the generation of$\cdot O_2^-$ due to the more negative CB than the $E(O_2/\cdot O_2^-)$. As shown in Fig. 4**c**, the DMPO-$\cdot O_2^-$ signal of $Bi_{19}S_{27}Br_3$/g-C_3N_4-5 composite exhibits the significantly higher intensity than the pure $Bi_{19}S_{27}Br_3$ and g-C_3N_4, indicating that more electron is generated by the photocatalytic reaction of $Bi_{19}S_{27}Br_3$/g-C_3N_4-5 compared with the pure $Bi_{19}S_{27}Br_3$ and g-C_3N_4. The time-resolved transient absorption spectroscopy (TAS) also confirms that with the introduction of $Bi_{19}S_{27}Br_3$, the $Bi_{19}S_{27}Br_3$/g-C_3N_4-5 composite performs the enhanced charge transfer efficiency (The detail is shown in Supplementary information and Fig. S15). Based on the above discussion, with the construction of C-S bridged Z-scheme heterojunction, more electron which generate on the g-C_3N_4 can transfer and gather on the $Bi_{19}S_{27}Br_3$. As a result, the C-S bridged Z-scheme $Bi_{19}S_{27}Br_3$/g-C_3N_4 composites exhibit the accelerated separation and transfer efficiency of photogenerated carriers. Besides, it also maintains the excellent reduction ability inherited from the $Bi_{19}S_{27}Br_3$. Therefore, the improving CO_2 photoconversion performance of $Bi_{19}S_{27}Br_3$/g-C_3N_4 composites can be obtained.

To explore the CO_2 adsorption ability of the materials, the models of CO_2 + g-C_3N_4, CO_2 + $Bi_{19}S_{27}Br_3$ and CO_2 + $Bi_{19}S_{27}Br_3$/g-C_3N_4 were further established to simulate the CO_2 adsorption process by the DFT calculation. As shown in Fig. 4**e**, after the optimization of the material structure, the CO_2 adsorption energy (E_{ads}) of $Bi_{19}S_{27}Br_3$ is calculated as −0.27 eV, which is higher than the E_{ads} of g-C_3N_4 (–0.15 eV). The E_{ads} of $Bi_{19}S_{27}Br_3$/g-C_3N_4 composite is calculated as −0.21 eV which is higher than that of g-C_3N_4, indicating the enhanced CO_2 adsorption capacity of $Bi_{19}S_{27}Br_3$/g-C_3N_4 composite compared with g-C_3N_4. Although the E_{ads} of $Bi_{19}S_{27}Br_3$/g-C_3N_4 composite is lower than $Bi_{19}S_{27}Br_3$, the unsatisfied charge carrier's separation efficiency seriously inhibits the photocatalytic CO_2 reduction activity of the pure $Bi_{19}S_{27}Br_3$. The in-situ DRIFTS measurement was applied to reveal the CO_2 photoreduction process on the surface of $Bi_{19}S_{27}Br_3$/g-C_3N_4 composite. In Fig. 4**f**, the peaks appearing at about 1250 and 1506 cm^{-1} belong to the symmetric C-O-C of b-CO_3^{2-} and m-CO_3^{2-} groups [53,54], respectively. On the other hand, the peak at 1678 cm^{-1} can be matched with asymmetric stretching of HCO_3^{-5}. The gradually increased peak at ~ 1560 cm^{-1} can be assigned to COOH* group (while the * is the adsorption state of catalyst) [53,55], which is an important intermediate during the photoreduction process of CO_2 to CO. Therefore, the possible reaction process of CO_2 photoreduction process on the $Bi_{19}S_{27}Br_3$/g-C_3N_4 material can be proposed. While the CO_2 molecule adsorbs on the $Bi_{19}S_{27}Br_3$/g-C_3N_4 composite, it reacts with the H^+ in water and photogenerated electron to generate the COOH* group. Then the COOH* group further reacts with the H^+ and photogenerated electron to generate the CO* . Finally, the CO molecule desorbs from the surface of catalyst.

4. Conclusion

In summary, a novel direct Z-scheme $Bi_{19}S_{27}Br_3$/g-C_3N_4 composite based on C-S bridge was successfully synthesized by the ionic liquid assisted solvent-thermal method. With the assistance of CS bonds, the photo-generated charges on the CB of g-C_3N_4 transfers to the VB of $Bi_{19}S_{27}Br_3$ through the C-S bonds rapidly. Therefore, the $Bi_{19}S_{27}Br_3$/g-C_3N_4 composites perform an enhanced CO_2 photoreduction activity for the yield of CO, which is about 4-times for pure g-C_3N_4 and 5-times for $Bi_{19}S_{27}Br_3$ material. Compared with the recent g-C_3N_4-based materials research (Table S3), the $Bi_{19}S_{27}Br_3$/g-C_3N_4 performs the relatively advanced CO_2 photoreduction activities without the addition of co-catalyst and sacrificial agent. Therefore, the construction of chemical bonds bridged direct Z-scheme is a promising strategy for precisely tailoring photogenerated charge separation direction of photocatalyst, providing a guidance for next-generation high efficiency photocatalyst in the field of green energy.

CRediT authorship contribution statement

J.X. Xia and J.Z. Zhao: Conceptualization, Methodology, Data curation. **J.Z. Zhao:** Data curation, Writing – original draft. **Z.R. Chen**: Validation, Formal analysis. **J. Zhong and Y.J. Li**: Validation. **M.X. Ji and S.Y. Wang**: Investigation, Writing – review & editing. **H.L. Chen and Y.X. Weng**: Visualization, Investigation. **H.M. Li and J.X. Xia**: Supervision, Project administration, Funding acquisition. All authors contributed to discussion and preparation of the manuscript.

Declaration of Competing Interest

The authors declare that they have no known competing financial interests or personal relationships that could have appeared to influence the work reported in this paper.

Acknowledgements

This work was financially supported by the National Natural Science Foundation of China (No. 22138011, 21676128, and 21878134) and Postgraduate Research & Practice Innovation Program of Jiangsu Province (KYCX19_1627). We thank SSRF for the support of XAS experiments.

Appendix A. Supporting information

Supplementary data associated with this article can be found in the online version at doi:10.1016/j.apcatb.2022.121162.

References

[1] S. Wang, X. Hai, X. Ding, S. Jin, Y. Xiang, P. Wang, B. Jiang, F. Ichihara, M. Oshikiri, X. Meng, Y. Li, W. Matsuda, J. Ma, S. Seki, X. Wang, H. Huang, Y. Wada, H. Chen, J. Ye, Intermolecular cascaded pi-conjugation channels for electron delivery powering CO_2 photoreduction, Nat. Commun. 11 (2020) 1149.

[2] W. Gao, S. Li, H. He, X. Li, Z. Cheng, Y. Yang, J. Wang, Q. Shen, X. Wang, Y. Xiong, Y. Zhou, Z. Zou, Vacancy-defect modulated pathway of photoreduction of CO_2 on single atomically thin $AgInP_2S_6$ sheets into olefiant gas, Nat. Commun. 12 (2021) 4747.

[3] Y. Xi, X. Zhang, Y. Shen, W. Dong, Z. Fan, K. Wang, S. Zhong, S. Bai, Aspect ratio dependent photocatalytic enhancement of $CsPbBr_3$ in CO_2 reduction with two-dimensional metal organic framework as a cocatalyst, Appl. Catal. B Environ. 297 (2021) 20411.

[4] Z. Wang, J. Fan, B. Cheng, J. Yu, J. Xu, Nickel-based cocatalysts for photocatalysis: hydrogen evolution, overall water splitting and CO_2 reduction, Mater. Today Phys. 15 (2020), 100279.

[5] X. Li, Y. Sun, J. Xu, Y. Shao, J. Wu, X. Xu, Y. Pan, H. Ju, J. Zhu, Y. Xie, Selective visible-light-driven photocatalytic CO_2 reduction to CH_4 mediated by atomically thin $CuIn_5S_8$ layers, Nat. Energy 4 (2019) 690–699.

[6] G. Liu, B. Wang, X. Zhu, P. Ding, J. Zhao, H. Li, Z. Chen, W. Zhu, J. Xia, Edge-site-rich ordered macroporous BiOCl triggers C=O activation for efficient CO_2 photoreduction, Small (2021), 2105228, https://doi.org/10.1002/smll.202105228.

[7] T. Kong, Y. Jiang, Y. Xiong, Photocatalytic CO_2 conversion: what can we learn from conventional CO_x hydrogenation? Chem. Soc. Rev. 49 (2020) 6579–6591.

[8] X. Lin, H. Jiang, C. Ma, Z. Zhu, X. Song, H. Wang, P. Huo, X. Li, Local surface plasma resonance effect enhanced Z-scheme ZnO/Au/g-C_3N_4 film photocatalyst for reduction of CO_2 to CO, Appl. Catal. B Environ. 283 (2021), 119638.
[9] J. Di, X. Zhao, C. Lian, M. Ji, J. Xia, J. Xiong, W. Zhou, X. Cao, Y. She, H. Liu, K. P. Loh, S.J. Pennycook, H. Li, Z. Liu, Atomically-thin Bi_2MoO_6 nanosheets with vacancy pairs for improved photocatalytic CO_2 reduction, Nano Energy 61 (2019) 54–59.
[10] Y. Wang, S. Wang, S. Zhang, X. Lou, Formation of hierarchical $FeCoS_2$-CoS_2 double-shelled nanotubes with enhanced performance for photocatalytic reduction of CO_2, Angew. Chem. Int. Ed. 59 (2020) 11918–11922.
[11] W. Wang, C. Deng, S. Xie, Y. Li, W. Zhang, H. Sheng, C. Chen, J. Zhao, Photocatalytic C-C coupling from carbon dioxide reduction on copper oxide with mixed-valence Copper(I)/Copper(II), J. Am. Chem. Soc. 143 (2021) 2984–2993.
[12] B. Wang, S. Yang, H. Chen, Q. Gao, Y. Weng, W. Zhu, G. Liu, Y. Zhang, Y. Ye, H. Zhu, H. Li, J. Xia, Revealing the role of oxygen vacancies in bimetallic $PbBiO_2Br$ atomic layers for boosting photocatalytic CO_2 conversion, Appl. Catal. B Environ. 277 (2020), 119170.
[13] J. Di, J. Xia, H. Li, Z. Liu, Freestanding atomically-thin two-dimensional materials beyond graphene meeting photocatalysis: opportunities and challenges, Nano Energy 35 (2017) 79–91.
[14] X. Jiao, K. Zheng, L. Liang, X. Li, Y. Sun, Y. Xie, Fundamentals and challenges of ultra-thin 2D photocatalysts in boosting CO_2 photoreduction, Chem. Soc. Rev. 49 (2020) 6592–6604.
[15] W.-J. Ong, L.-L. Tan, Y.H. Ng, S.-T. Yong, S.-P. Chai, Graphitic carbon nitride (g-C_3N_4)-based photocatalysts for artificial photosynthesis and environmental remediation: are we a step closer to achieving sustainability? Chem. Rev. 116 (2016) 7159–7329.
[16] D. Huang, Z. Li, G. Zeng, C. Zhou, W. Xue, X. Gong, X. Yan, S. Chen, W. Wang, M. Cheng, Megamerger in photocatalytic field: 2D g-C_3N_4 nanosheets serve as support of 0D nanomaterials for improving photocatalytic performance, Appl. Catal. B Environ. 240 (2019) 153–173.
[17] W. Li, L. Jin, F. Gao, H. Wan, Y. Pu, X. Wei, C. Chen, W. Zou, C. Zhu, L. Dong, Advantageous roles of phosphate decorated octahedral CeO_2 {111}/g-C_3N_4 in boosting photocatalytic CO_2 reduction: charge transfer bridge and Lewis basic site, Appl. Catal. B Environ. 294 (2021), 120257.
[18] J. Fu, Q. Xu, J. Low, C. Jiang, J. Yu, Ultra-thin 2D/2D WO_3/g-C_3N_4 step-scheme H_2-production photocatalyst, Appl. Catal. B Environ. 243 (2019) 556–565.
[19] X. Zhang, T. Wu, C. Yu, R. Lu, Ultrafast interlayer charge separation, enhanced visible-light absorption, and tunable overpotential in twisted graphitic carbon nitride bilayers for water splitting, Adv. Mater. 33 (2021), 2104695.
[20] G. Liu, C. Zhen, Y. Kang, L. Wang, H. Cheng, Unique physicochemical properties of two-dimensional light absorbers facilitating photocatalysis, Chem. Soc. Rev. 47 (2018) 6410–6444.
[21] P. Xia, M. Antonietti, B. Zhu, T. Heil, J. Yu, S. Cao, Designing defective crystalline carbon nitride to enable selective CO_2 photoreduction in the gas phase, Adv. Funct. Mater. 29 (2019), 1900093.
[22] Y. Li, B. Li, D. Zhang, L. Cheng, Q. Xiang, Crystalline carbon nitride supported copper single atoms for photocatalytic CO_2 reduction with nearly 100% CO selectivity, ACS Nano 14 (2020) 10552–10561.
[23] M. Shen, L. Zhang, M. Wang, J. Tian, X. Jin, L. Guo, L. Wang, J. Shi, Carbon-vacancy modified graphitic carbon nitride: enhanced CO_2 photocatalytic reduction performance and mechanism probing, J. Mater. Chem. A 7 (2019) 1556–1563.
[24] P. Sharma, S. Kumar, O. Tomanec, M. Petr, J. Zhu Chen, J.T. Miller, R.S. Varma, M. B. Gawande, R. Zboril, Carbon nitride-based ruthenium single atom photocatalyst for CO_2 reduction to methanol, Small 17 (2021), 2006478.
[25] J. Di, J. Xia, X. Li, M. Ji, H. Xu, Z. Chen, H. Li, Constructing confined surface carbon defects in ultra-thin graphitic carbon nitride for photocatalytic free radical manipulation, Carbon 107 (2016) 1–10.
[26] L. Cheng, H. Yin, C. Cai, J. Fan, Q. Xiang, Single Ni atoms anchored on porous few-layer g-C_3N_4 for photocatalytic CO_2 reduction: the role of edge confinement, Small 16 (2020), 2002411.
[27] C. Wang, X. Yi, P. Wang, Powerful combination of MOFs and C_3N_4 for enhanced photocatalytic performance, Appl. Catal. B Environ. 247 (2019) 24–48.
[28] R. Zhang, P. Li, F. Wang, L. Ye, A. Gaur, Z. Huang, Z. Zhao, Y. Bai, Y. Zhou, Atomically dispersed Mo atoms on amorphous g-C_3N_4 promotes visible-light absorption and charge carriers transfer, Appl. Catal. B Environ. 250 (2019) 273–279.
[29] N. Tian, K. Xiao, Y. Zhang, X. Lu, L. Ye, P. Gao, T. Ma, H. Huang, Reactive sites rich porous tubular yolk-shell g-C_3N_4 via precursor recrystallization mediated microstructure engineering for photoreduction, Appl. Catal. B Environ. 253 (2019) 196–205.
[30] M. Ismael, A review on graphitic carbon nitride (g-C_3N_4) based nanocomposites: synthesis, categories, and their application in photocatalysis, J. Alloy. Compd. 846 (2020), 156446.
[31] Q. Xu, L. Zhang, J. Yu, S. Wageh, A. Al-Ghamdi, M. Jaroniec, Direct Z-scheme photocatalysts: principles, synthesis, and applications, Mater. Today 21 (2018) 1042–1063.
[32] M. Ou, W. Tu, S. Yin, W. Xing, S. Wu, H. Wang, S. Wan, Q. Zhong, R. Xu, Amino-assisted anchoring of $CsPbBr_3$ perovskite quantum dots on porous g-C_3N_4 for enhanced photocatalytic CO_2 reduction, Angew. Chem. Int. Ed. 41 (2018) 13570–13574.
[33] Z. Jiang, W. Wan, H. Li, S. Yuan, H. Zhao, P. Wong, A hierarchical Z-scheme alpha-Fe_2O_3/g-C_3N_4 hybrid for enhanced photocatalytic CO_2 reduction, Adv. Mater. 30 (2018), 1706108.
[34] C. Wang, Y. Zhao, H. Xu, Y. Li, Y. Wei, J. Liu, Z. Zhao, Efficient Z-scheme photocatalysts of ultrathin g-C_3N_4-wrapped Au/TiO_2-nanocrystals for enhanced visible-light-driven conversion of CO_2 with H_2O, Appl. Catal. B Environ. 263 (2020), 118314.
[35] W. Zhang, A. Mohamed, W. Ong, Z-Scheme photocatalytic systems for carbon dioxide reduction: where are we now? Angew. Chem. Int. Ed. 51 (2020) 22894–22915.
[36] P. Zhou, J. Yu, M. Jaroniec, All-solid-state Z-scheme photocatalytic systems, Adv. Mater. 26 (2014) 4920–4935.
[37] X. Wang, X. Wang, J. Huang, S. Li, A. Meng, Z. Li, Interfacial chemical bond and internal electric field modulated Z-scheme S_v-$ZnIn_2S_4$/$MoSe_2$ photocatalyst for efficient hydrogen evolution, Nat. Commun. 12 (2021) 4112.
[38] M. Zhang, M. Lu, Z.L. Lang, J. Liu, M. Liu, J.N. Chang, L.Y. Li, L.J. Shang, M. Wang, S.L. Li, Y.Q. Lan, Semiconductor/covalent-organic-framework Z-Scheme heterojunctions for artificial photosynthesis, Angew. Chem. Int. Ed. 59 (2020) 6500–6506.
[39] W. Xu, W. Tian, L. Meng, F. Cao, L. Li, Interfacial chemical bond-modulated Z-scheme charge transfer for efficient photoelectrochemical water splitting, Adv. Energy Mater. 11 (2021), 2003500.
[40] P. Zhang, L. Wu, W. Pan, S. Bai, R. Guo, Efficient photocatalytic H_2 evolution over NiS-PCN Z-scheme composites via dual charge transfer pathways, Appl. Catal. B Environ. 289 (2021), 120040.
[41] Z. Wu, Y. Liu, S. Zhang, Z. Huang, Q. Jiang, T. Zhou, J. Hu, Biomimetic structure design and construction of cactus-like MoS_2/$Bi_{19}Cl_3S_{27}$ photocatalysts for efficient hydrogen evolution, J. Mater. Chem. A 6 (2018) 21404–21409.
[42] L. Ai, L. Wang, M. Xu, S. Zhang, N. Guo, D. Jia, L. Jia, Defective $Bi_{.333}(Bi_6S_9)Br$/Bi_2S_3 heterostructure nanorods: boosting the activity for efficient visible-light photocatalytic Cr(VI) reduction, Appl. Catal. B Environ. 284 (2021), 119730.
[43] Y. Chen, G. Tian, T. Feng, W. Zhou, Z. Ren, T. Han, Y. Xiao, H. Fu, Single-crystalline $Bi_{19}Br_3S_{27}$ nanorods with efficiently improved photocatalytic activity, CrystEngComm 17 (2015) 6120–6126.
[44] J. Li, W. Pan, Q. Liu, Z. Chen, Z. Chen, X. Feng, H. Chen, Interfacial engineering of $Bi_{19}Br_3S_{27}$ nanowires promotes metallic photocatalytic CO_2 reduction activity under near-infrared light irradiation, J. Am. Chem. Soc. 143 (2021) 6551–6559.
[45] Z. Chen, Z. Wu, Z. Song, X. Zhang, H. Yang, Q. Jiang, T. Zhou, N. Liu, J. Hu, Crucial effect of halogen on the photocatalytic hydrogen evolution for $Bi_{19}X_3S_{27}$ (X = Cl, Br) nanomaterials, Ind. Eng. Chem. Res. 58 (2019) 22958–22966.
[46] C. Deng, H. Guan, X. Tian, Novel $Bi_{19}S_{27}Br_3$ superstructures: facile microwave-assisted aqueous synthesis and their visible light photocatalytic performance, Mater. Lett. 108 (2013) 17–20.
[47] Y. Wang, Y. Tian, L. Yan, Z. Su, DFT study on sulfur-doped g-C_3N_4 nanosheets as a photocatalyst for CO_2 reduction reaction, J. Phys. Chem. C 122 (2018) 7712–7719.
[48] C. Min, Y. Yang, H. Liang, Z. He, J. Zhu, Q. Li, Covalently bonded 2D/0D g-C_3N_4/MoS_2 nanocomposites for enhanced tribological properties in oil, ChemistrySelect 6 (2021) 1661–1668.
[49] J. Li, G. Zhan, Y. Yu, L. Zhang, Superior visible light hydrogen evolution of Janus bilayer junctions via atomic-level charge flow steering, Nat. Commun. 7 (2016) 11480.
[50] J. Di, J. Xia, M. Chisholm, J. Zhong, C. Chen, X. Cao, F. Dong, Z. Chi, H. Chen, Y. Weng, J. Xiong, S. Yang, H. Li, Z. Liu, S. Dai, Defect-tailoring mediated electron-hole separation in single-unit-cell Bi_3O_4Br nanosheets for boosting photocatalytic hydrogen evolution and nitrogen fixation, Adv. Mater. 31 (2019), 1807576.
[51] Y. Zhang, B. Xia, J. Ran, K. Davey, S. Qiao, Atomic-level reactive sites for semiconductor-based photocatalytic CO_2 reduction, Adv. Energy Mater. 10 (2020), 1903879.
[52] Y. Wang, X. Shang, J. Shen, Z. Zhang, D. Wang, J. Lin, J. Wu, X. Fu, X. Wang, C. Li, Direct and indirect Z-scheme heterostructure-coupled photosystem enabling cooperation of CO_2 reduction and H_2O oxidation, Nat. Commun. 11 (2020) 3043.
[53] B. Wang, J. Zhao, H. Chen, Y.-X. Weng, H. Tang, Z. Chen, W. Zhu, Y. She, J. Xia, H. Li, Unique Z-scheme carbonized polymer dots/$Bi_4O_5Br_2$ hybrids for efficiently boosting photocatalytic CO_2 reduction, Appl. Catal. B Environ. 293 (2021), 120182.
[54] J. Di, C. Zhu, M. Ji, M. Duan, R. Long, C. Yan, K. Gu, J. Xiong, Y. She, J. Xia, H. Li, Z. Liu, Defect-Rich $Bi_{12}O_{17}Cl_2$ nanotubes self-accelerating charge separation for boosting photocatalytic CO_2 reduction, Angew. Chem. Int. Ed. 57 (2018) 14847–14851.
[55] Wu X. Li, W. Shi, P. Ling, Y. Sun, X. Jiao, S. Gao, L. Liang, J. Xu, W. Yan, C. Wang, Y. Xie, Efficient visible-light-driven CO_2 reduction mediated by defect-engineered BiOBr atomic layers, Angew. Chem. Int. Ed. 57 (2018) 8719–8723.